ELSEVIER

Tectonophysics 352 (2002) 275–293

TECTONOPHYSICS

www.elsevier.com/locate/tecto

Experiments simulating surface deformation induced by pluton emplacement

V. Acocella [a,*], G. Mulugeta [b]

[a] *Dipartimento Scienze Geologiche, Università Roma Tre, Largo San L. Murialdo, 1, 00146 Rome, Italy*
[b] *Institute of Earth Sciences, Norbyvagen 18B, S-75236 Uppsala, Sweden*

Received 16 August 2001; accepted 18 April 2002

Abstract

We present centrifuge experiments to study the surface deformation induced by shallow pluton emplacement in a rheologically stratified crust. Sand simulates the topmost brittle crust; plastilina and denser silicone represent more and less competent crustal portions, respectively; lighter silicone simulates a buoyant intrusion. In the models, density differences affect the rate of intrusion but not their evolution or shape, whereas viscosity and strength stratifications control both the shape and rate of the intrusions. With a higher viscosity contrast (10^{2-4}) between the intrusion and the embedding media, the rise of the lighter silicone induces a laccolith-like intrusion, responsible for doming and thinning of the overburden; an apical depression may form, inducing silicone extrusion. Conversely, with a lower (10^{1}) viscosity contrast, the overburden and the intrusion exhibit a lens-shaped form, with a broad central depression bordered by an upward flexure towards the periphery. A sag in the floor of the intrusion is commonly observed; no silicone extrusion occurred. The intrusion is a hybrid between a laccolith and a lopolith. The comparison with nature (1) confirms roof uplift as an important means of accommodating space during pluton emplacement and (2) suggests that, where roof uplift plays a major role, pluton emplacement can induce a well-correlated sequence of events at surface: doming, the development of a depression and extrusion.

Keywords: Pluton emplacement; Surface deformation; Analogue modelling

1. Introduction

The mechanisms of the rise and emplacement of plutons have been mainly studied, in the last 30 years, by means of geological data (Pitcher, 1979; Bateman, 1984; Castro, 1987; Hutton, 1988; Ramsay, 1989; Brown, 1994), analogue (Berner et al., 1972; Dixon, 1975; Whitehead and Luther, 1975; Ramberg, 1981; Schmeling et al., 1988; Cruden, 1990) and numerical models (Mahon et al., 1988; Bittner and Schmeling, 1995; Hanson and Glazner, 1995; Weinberg and Podladchikov, 1995). In the last decade, many studies have focused on the mechanism of pluton emplacement with regard to the role of regional tectonics (Glazner, 1991; D'Lemos et al., 1992; McCaffrey 1992; Tikoff and Teyssier, 1992; Tobisch and Cruden, 1995; Vigneresse, 1995; Tikoff and de Saint Blanquat, 1997; Roman Berdiel et al., 1997; Benn et al., 1998).

Several attempts have been made to study the deformation due to of pluton emplacement, mainly

* Corresponding author. Tel.: +39-06-54888027; fax: +39-06-54888201.
E-mail address: acocella@uniroma3.it (V. Acocella).

0040-1951/02/$ - see front matter
PII: S0040-1951(02)00218-4

evaluating the interaction between local and regional strain (Brun and Pons, 1981; Paterson et al., 1989; Petford and Atherton, 1992; Guglielmo, 1993; Wilson and Grocott, 1999) or the general relations between plutonism and associated doming and volcanism (Lipman, 1984; Shaw, 1985; Yoshida, 2001). The study of the surface deformation induced by pluton emplacement has received less attention. Since the erosion of the overburden during and after pluton emplacement limits field observations, few attempts have been made to consider the roof deformation induced by plutons (Morgan et al., 1998; Grocott et al., 1999; Acocella, 2000). Since several papers have recently shown that roof lifting is a viable mechanism to accommodate space (Scaillet et al., 1995; Brown and Solar, 1998; Cruden, 1998; Hogan et al., 1998; Morgan et al., 1998; Quirk et al., 1998; Grocott et al., 1999; Acocella, 2000), the limitation due to erosion in evaluating the surface deformation might be crucial in defining the mechanism of pluton emplacement.

Experimental studies on the surface deformation induced by intrusions have been mainly carried out with application to volcanic areas, simulating elastic and anelastic deformation (Withjack and Scheiner, 1982; Dixon and Simpson, 1987; Schultz-Ela et al., 1993; Marti et al., 1994; Roman-Berdiel et al., 1995; Donnadieu and Merle, 1998; Acocella et al., 2001).

The aim of this paper is to study the surface deformation induced by pluton emplacement as a consequence of viscosity/strength contrasts between intrusion and the embedding media. Models with a higher viscosity contrast (10^{2-4}) show an evolutionary sequence where a laccolith-like intrusion induces doming, the development of a crestal depression and extrusion. Conversely, a lower viscosity contrast (10^{1}) between the intrusive body and the confining substratum results in lens-shaped forms of the intrusions beneath a region of broad downwarp; the intrusion is a hybrid between a laccolith and lopolith. The experiments are briefly compared with nature, confirming roof uplift as an important means of accommodating space during pluton emplacement.

2. Experimental procedure

2.1. Set-up

Analogue models, simulating pluton emplacement, were run by introducing rheologically stratified sample layers in a cylindrical cavity in a centrifuge. Models were run in a centrifuge to scale body forces in relation to surface forces. The sample contained materials such as low-cohesion sand (simulating the upper part of the brittle crust, i.e., sedimentary layers), overlying a denser silicone putty (DSI, used as a ductile layer analogue, i.e., decollement levels), plastilina (simulating a more viscous and denser crustal layer, i.e., basement) and a lighter silicone putty (LSI, simulating the intrusion). The centrifuge was run at approximately 10^{3} g, inducing, through a density contrast, the rise of the LSI through the DSI up to the base of the sand pack.

Three configurations were adopted for the materials within the sample cylinder, in order to test different material properties and boundary conditions. All the configurations (Fig. 1) are characterised by an upper sand layer (diameter = 9 cm, thickness 0–2 cm), an underlying layer of DSI (diameter = 9 cm, thickness 0–2 cm) and a bottom layer of LSI (diameter 1–3 cm, thickness 1–4 cm). Configuration A (used in 18 experiments) is characterized by a plastilina ring bordering the LSI and an additional basal layer of LSI (diameter = 9 cm, thickness = 0.5 cm; Fig. 1a). Configuration B (three experiments) is similar to A, except for the absence of the basal layer of LSI (Fig. 1b). Configuration C (four experiments) is characterized by denser silicone bordering the LSI and thus replacing the plastilina ring (Fig. 1c).

In the models, the contrast in viscosity and/or strength between the intruding body and the confining medium is moderate, with effective viscosity ratios in the range $10–10^{4}$. We do not consider the emplacement of fluid-like intrusions with higher viscosity contrast with regard to the confining medium, as this is not easily satisfied by currently available experi-

Fig. 1. Section view of the experimental set-up for model configurations A, B, C. The imposed and observed conditions of the experiments are reported below. D/B = ratio between the thickness of the ductile and brittle materials; duration = duration of the experiment; intrusion = dimensions (height × diameter) of the cylindrical intrusion; W, H, A dome = final width, height, aspect ratio (width/height) of the dome; A diapir = aspect ratio (width/height) of the intrusion; extrusion times: times required to observe extrusion of LSI in the experiments, where this occurred.

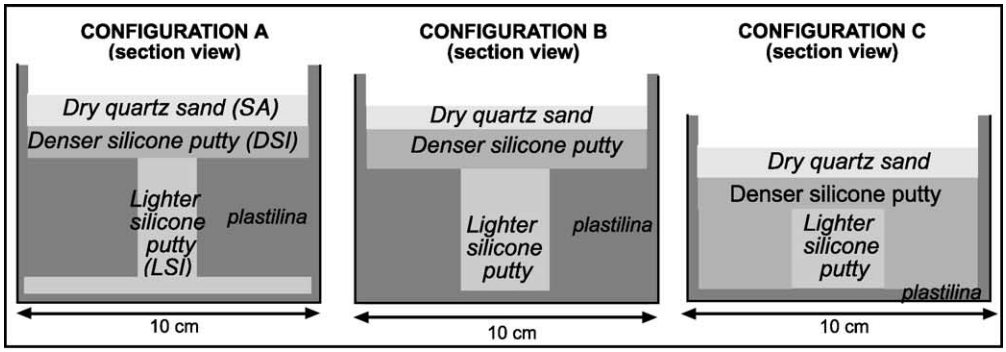

		imposed conditions			observed conditions				
experiment & configuration		D/B	duration	intrusion (cm)	W dome (mm)	H dome (mm)	A dome	A diapir	extrusion times
DOM 1	B	1.5	15 sec	4 x 3	50	3	16.7	9.5	
DOM 2	B	1.5	30 sec	4.5 x 3	60	5	12	6.7	
DOM 3	A	1.5	60 sec	4.5 x 3	80	6	13.3	8	60 sec
DOM 4	A	1.5	30 sec	3.5 x 2	52	4	13	6	30 sec
DOM 5	B	1.5	75 sec	4 x 1	55	4	13.8	7.9	
DOM 6	A	3	20 sec	3.5 x 2	35	4	8.8	5.7	20 sec
DOM 7	A	1	90 sec	4 x 2	70	5	14	9.3	75 sec
DOM 8	A	1.5	60 sec	4 x 3	68	3	22.7	9	60 sec
DOM 9	A	0.5	60 sec	4 x 2	75	4.5	17.6	6.4	60 sec
DOM 10	A	0	15 sec	4 x 2	52	10	5.2		10 sec
DOM 11	A	4	15 sec	4 x 2	44	3.5	12.6	6.9	10 sec
DOM 12	A	4	7 sec	4 x 2	44	4	11	4.5	7 sec
DOM 13	A	0	3 sec	4 x 2	38	3.5	10.9	5.4	
DOM 14	A	0.5	30 sec	4 x 2	63	3	20	12	30 sec
DOM 15	A	1	30 sec	4 x 2	61	4	15.3	6.6	30 sec
DOM 16	C	1	60 sec	2.5 x 2	71	2	35.5	15	
DOM 17	C	2	30 sec	2 x 3	44	1.5	29.3	15	
DOM 18	C	2	30 sec	3 x 3	77	4	19.3	14	30 sec
DOM 19	C	2	15 sec	3 x 3	68	2.5	27	11	
DOM 20	A	1	150 sec	1 x 2	73	3.5	20.9	15	
DOM 21	A	1	120 sec	2.5 x 2	72	4	18	9	
DOM 22	A	1	120 sec	4 x 1.7	71	3.5	20.3	12	
DOM 23	A	infinite	15 sec	2 x 4	37	4	9.3	4.7	7 sec
DOM 24	A	infinite	60 sec	2 x 4	79	1	79		
DOM 25	A	infinite	60 sec	2 x 4	70	1	140		

mental materials (e.g., Ramberg, 1981, p. 332). The adopted moderate viscosity contrast between the intrusion and the embedding media requires (Rubin, 1993) a diapiric ascent of the intrusive material. Thus, the styles of overburden deformation in the models are a result of diapiric emplacement and interaction with the overburden.

In order to focus on the deformation due to intrusion emplacement, we simulated pluton emplacement as exclusively due to buoyancy forces by diapiric ascent, without introducing a far-field stress. Nevertheless, the set up of the apparatus introduced a limited amount of lateral extension, estimated as 3% of the diameter of the cylinder.

We varied the thickness B of the sand and the thickness D of the DSI, expressed by the ratio D/B, the dimensions (height and diameter) of the LSI layer and the duration of the experiment (from 30 to 180 s).The surface deformation was measured every 15 s by means of section photos with a scale bar (error $\pm$ 1 mm). The centrifuge times here considered are the times in which the centrifuge reached a steady rotation state and do not include acceleration or deceleration times. Upon completion of an experiment, the model was impregnated with water and then sliced to observe the final deformation in cross-section.

2.2. Scaling and materials

We performed dynamic scaling of models, following the principles discussed by Hubbert (1937) and Ramberg (1981). We chose (Table 1) a length ratio between model and nature $L^* = 10^{-6}$ (1 cm of the model corresponding to $\approx$ 10 km in nature).

Table 1
Model ratios applicable to the present study

Parameter	Model ratio
Length	$L^* \approx 10^{-6}$
Density	$\rho^* \approx 0.5$
Gravity	$g^* \approx 10^3$
Stress	$\sigma^* \approx 10^{-4}$
Viscosity (variable)[a]	$\mu^* \approx 10^{-10}$
Time	$t^* = \mu^*/\sigma^* \approx 10^{-6}$

[a] This ratio assumes a prototype viscous magma of $\mu \approx 10^{14}$ Pa s as equivalent to an experimental magma of $\mu \approx 10^4$ Pa s.

The densities of natural rocks (2000–2700 kg/m^{-3}) and of the experimental materials (900–1800 kg/m^{-3}) impose a density ratio $\rho^* \sim 0.5$. Since the models were run at $10^3 g$, the gravity ratio is $g^* = 10^3$. These ratios imply that the stress ratio between model and nature is $\sigma^* = \rho g L \sim 5 \times 10^{-4}$ (Table 1).

We assumed a Mohr–Coulomb failure criterion for the rocks in the upper part of the brittle crust, with an angle of internal friction $\phi = 30°$ and a mean cohesion $c \sim 10^6$–10^7 Pa. Thus, in the models, cohesion, having the dimension of stress, was scaled down by a factor of $\sim 5 \times 10^{-4}$; this required use of materials with $c \sim 10^2$–10^3 Pa to simulate the upper part of the brittle crust.

For this purpose, we used low-cohesion sand, with density = 1400 kg/m^3, $\phi = 35°$ and $c \sim 100$–1000 Pa under the imposed gravity ($10^3 g$) and the related normal stresses ($\sim 10^4$ Pa). The rheological properties of the sand and its use as analogue material are discussed in Mandl et al. (1977), Krantz (1991) and Schellart (2000).

The simulation of pluton emplacement has to consider the viscosities and the related strain rates and time scales. Magma viscosities can vary within 13 orders of magnitude, as a function of a limited range of temperatures and water content (Table 1; Talbot, 1999). Here, we simulate a magma with a high viscosity, which varies within a wide range (10^8–10^{16} Pa s) depending on its cooling rate and crystallization: As a consequence, the time factor calculated is dependent on the assumed viscosity ratio (Table 1). Silicone putty can be used to simulate the ductile behaviour of magma (e.g., Merle and Vendeville, 1995; Merle, 1998). Here, Newtonian lighter silicone putty (LSI), with a density of 1310 kg/m^3 and viscosity $\eta = 2 \times 10^4$ Pa s simulated the intrusion (Hailermariam and Mulugeta, 1998, and references therein).

The ductile layers of the upper and intermediate crust have been simulated using a denser silicone (DSI; density = 1410 kg/m^3; viscosity $\eta \approx 3 \times 10^5$ Pa s); this was made denser by adding painter's putty (fönsterKitt, bought from Beckers färg, Stockholm, Sweden).

For models of configurations A and B, plastilina, with a yield strength of $\approx 2 \times 10^5$ Pa and creep viscosity $\eta = 10^7$–10^8 Pa s (depending on strain rate),

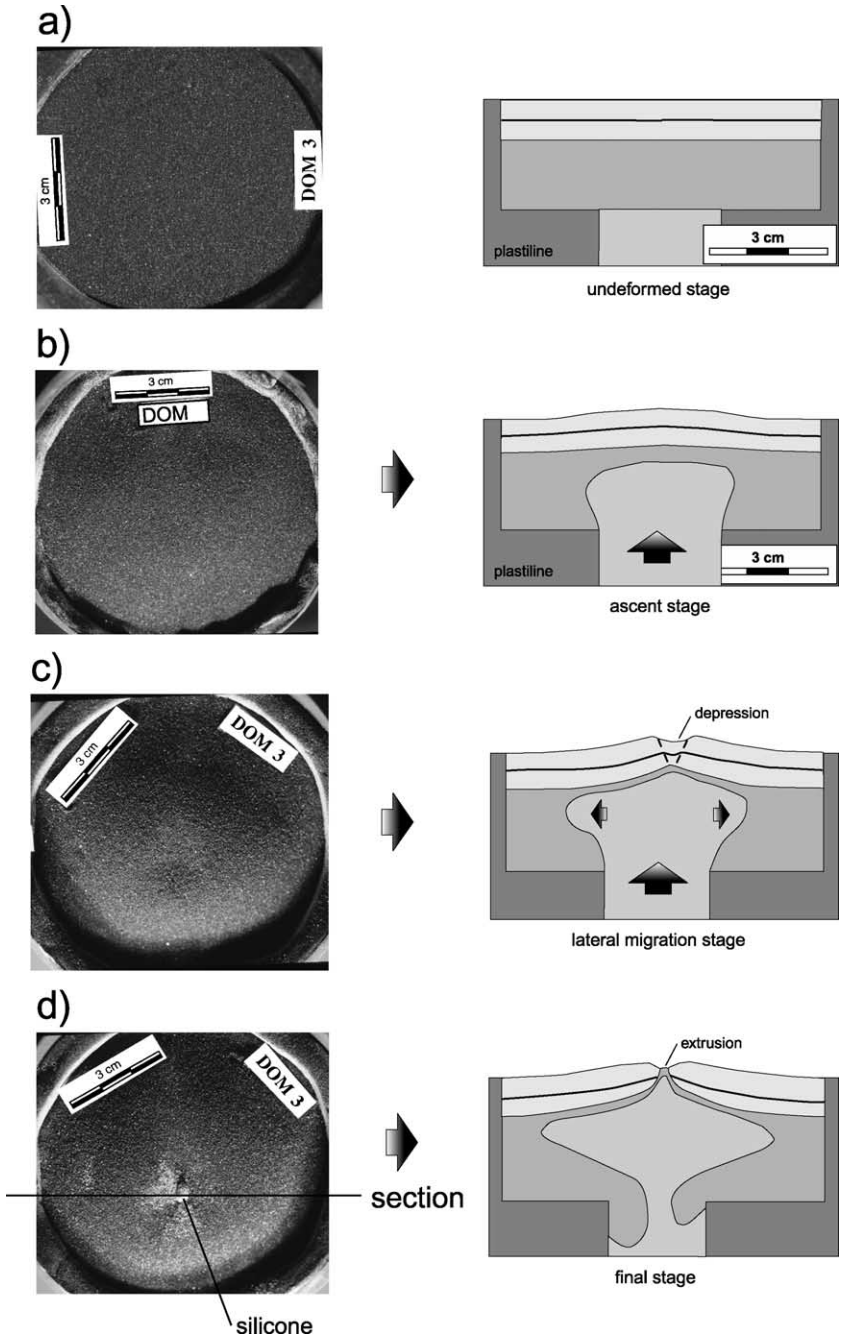

Fig. 2. Progressive evolution of experiment DOM 3 (configuration A) depicting map and section views at intervals of 15 s. (a) Undeformed stage. (b) Dome formation. (c) Nucleation of an apical depression. (d) Silicone putty extrusion within the depression.

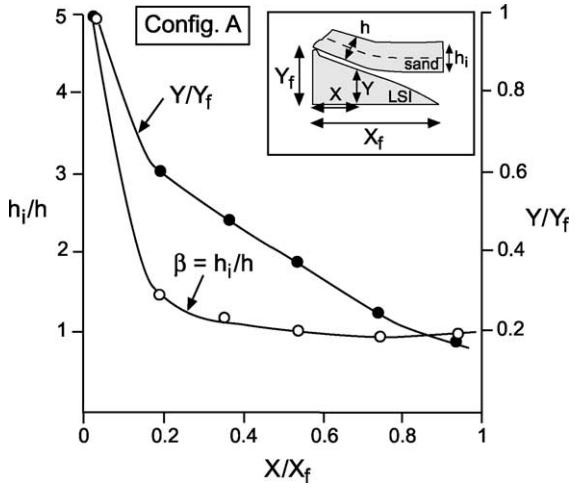

Fig. 3. Relationships between intrusion emplacement and surface deformation in DOM 3. The deformation in the sand is expressed by a stretch parameter $\beta = h_i/h$, where h_i is the initial thickness and h is the final thickness. Shape variation of the intrusion is given by $\kappa = Y/Y_f$, where Y is the thickness of the intrusion and Y_f is its maximum thickness. These are plotted outwards as a function of dimensionless radial distance (X/X_f, where X is the distance from the centre of the intrusion and X_f is the maximum distance). Measures taken from section in Fig. 2d.

simulated a more viscous and stronger ductile crust. Plastilina (bought from Uppsala färg, Sweden) is a mixture of clay powder, waxes, oil and colour.

According to the used length ratio, sand corresponds to the upper sedimentary part of a brittle crust, 5–10 km thick, overlying ductile decollement layers (silicone), 0–10 km thick and more viscous and stronger ductile basement layers (plastilina), 0–30 km thick. The source of the analogue magma is underneath, that is in the lower part of the crust. Thus, the experiments are believed to represent the ascent of magma from the lower crust within an upper crust with a thickness of very few tens of km.

The extent of applicability of the experimental results is limited by the knowledge of such natural parameters as viscosities, time scales and strain rates. The aim of the experiments is not to simulate a specific case, as the impossibility of determining its natural parameters would limit the applicability of the models. The goal is rather to understand the overall mechanism of deformation, which might be valid for a wide range of natural cases.

3. Results

3.1. Evolution of the experiments with configuration A

The experiments with configuration A have a higher ($\Delta\eta \approx 10^{2-4}$) viscosity contrast between the buoyant material and the embedding media (Fig. 1) and are here shown through a representative model (DOM 3; initial conditions in Fig. 1).

Fig. 2a shows the map view of the undeformed model. A dome (5 cm wide and 4 mm high) forms at

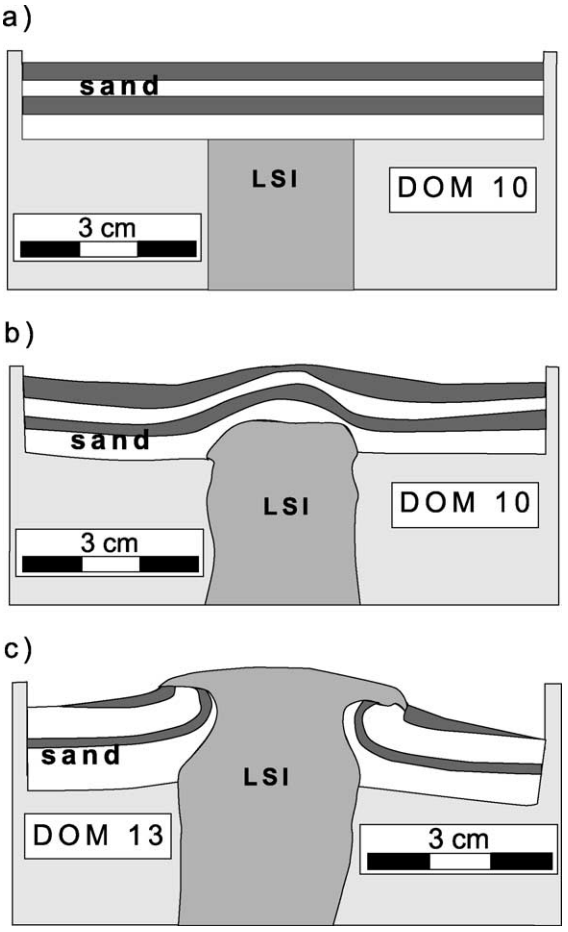

Fig. 4. Evolution of two experiments characterized by the same initial configuration and absence of the DSI layer. (a) Initial set-up, section view. (b) Section of the model after 3 s of centrifuge. (c) Section of a model with the same initial configuration after 15 s.

surface after 15 seconds (s) of centrifuge (Fig. 2b). At 30 s, the dome has increased its dimensions (height = 6 mm, width = 6 cm) and a depression, ~ 1 mm deep, starts to form on its crest (Fig. 2c). At depth (section in Fig. 2c), the LSI reaches the base of the sand layer and starts to spread laterally. The depression is bordered by inward dipping normal faults. At 60 s, the dome is 8 cm wide, with a constant maximum height of 6 mm (Fig. 2d). The depth of the apical depression increased to 2 mm, with a width ~ 1.5 cm. Silicone begins to intrude the apical depression, reaching surface. In the section (Fig. 2d), the LSI has completely spread at the base of the sand layer, showing a mushroom-like shape with a domed roof; its roots are bordered by the sinking DSI.

Fig. 3 shows the final variation in the thickness of the overburden and the intrusion in section view (data taken from Fig. 2d). The deformation in the sand is expressed by a stretch parameter $\beta = h_i/h$, which is the ratio of initial (h_i) to final (h) thickness. Shape variation of the intrusion is given by $\kappa = Y/Y_f$, where y is the thickness of the intrusion at a distance X from its centre and Y_f is the maximum thickness. These are plotted outwards as a function of dimensionless radial distance (X/X_f, where X_f is the maximum distance from the centre of the intrusion). Rising of the intrusion induces the flexuring and thinning of the overburden. The intrusion is thickest in its central portion, corresponding to the maximum thinning of the overburden (Fig. 3).

The evolution of DOM 3 is consistent with the other experiments with configuration A. The complete evolution of these experiments is characterized by: (a) doming; (b) the development of a crestal depression; (c) the extrusion of the LSI within the depression.

Minor variations from this evolution occur depending upon the imposed conditions. Removing the DSI layer introduces variations in the shape of the intru-

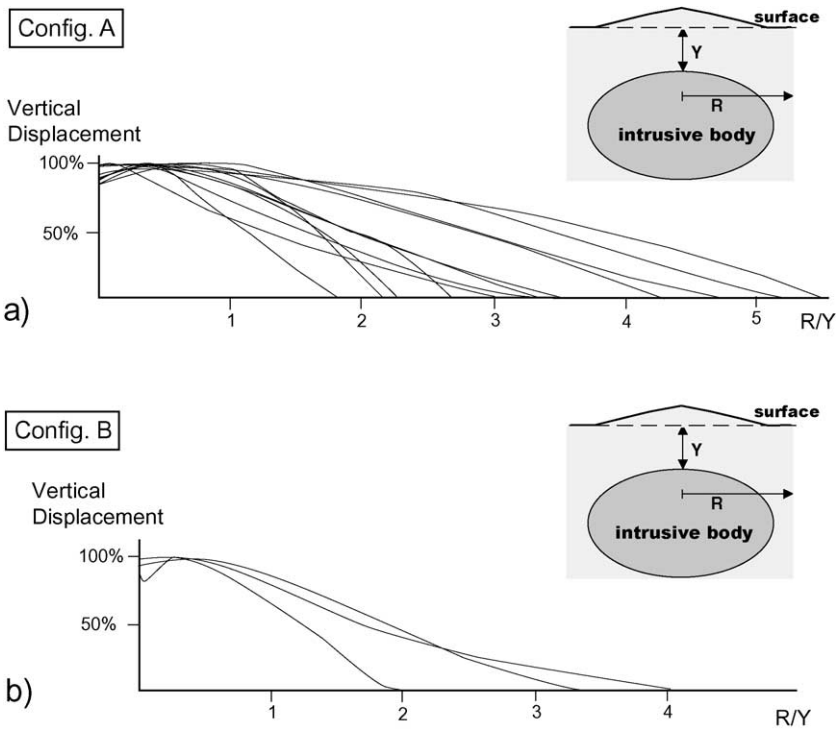

Fig. 5. (a) Uplift profiles of half of the experimental domes in different experiments with configuration A as a function of the distance from the centre of the dome. The uplift is normalized to the maximum uplift (100%) and the distance is normalized to the initial depth of the intrusion. (b) Uplift profiles of half of the experimental domes with configuration B as a function of the distance from the centre of the dome.

sion. In Fig. 4, we show the evolution of two models with the same imposed conditions. Fig. 4a shows a section of the initial set-up of the experiments, characterized by the lack of the DSI. After 3 s of centrifuge, the LSI punches up through the brittle sand layer, forming a dome at surface (Fig. 4b). A model with the same initial configuration, after 15 s, is shown in Fig. 4c. Even though the LSI extruded, similarly to that observed in DOM 3, it forms a wider plug, with an almost constant diameter. The reverse drags in the sand partially accommodate the required space for the rise of the plug. No lateral spreading of the LSI has been observed at the contact between the plastilina and the sand; thus, laccolith-like geometries of the LSI were not observed in the absence of the DSI layer.

The normalized profiles of half of the experimental domes with configuration A at the final stage of deformation are shown in Fig. 5a. The variation of the uplift from the crest of the dome is a function of the maximum uplift (*Y*-axis, corresponding to 100%) along a radial distance (*X*-axis; see inset in Fig. 5a). Fig. 5a shows the uplift variation in domes with and without apical depression; the depth of the depression is always less than 20% the maximum uplift. Curves showing an upward convexity are related to experiments without extrusion; curves with a downward convexity are related to experiments with extrusion. Thus, the downward convexity of the curves is the result of the upward push induced by the extruding silicone.

3.2. Evolution of the experiments with configuration B

The set-up of the experiments with configuration B is identical to the one of the experiments with configuration A, except for the absence of the basal layer of LSI (Fig. 1b).

Similarly to DOM 3 (configuration A), the evolution of the experiments with configuration B (not shown here) is characterized by doming, the development of a crestal depression and apical extrusion of

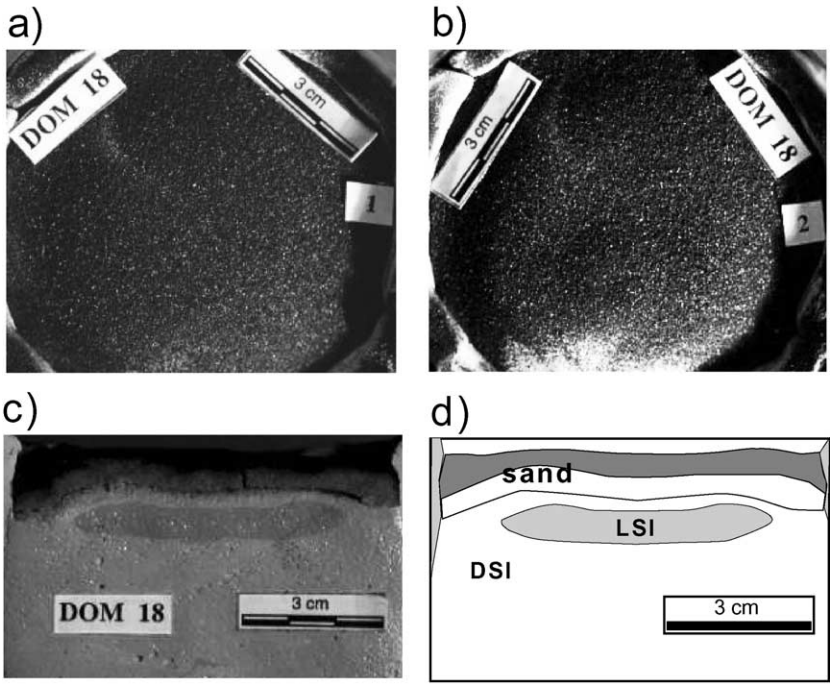

Fig. 6. Evolution of DOM 18 experiment with configuration C. (a) Map view of the experiment at $t = 15$ s, showing dome formation at surface. (b) Map view and (c) cross-section of the experiment at $t = 30$ s; the dome shows a broad central depression. (d) Line drawing of the cross section in (c).

silicone. The normalized profiles of half of the domes with configuration B at the final stage of deformation are shown in Fig. 5b. Similarly to Fig. 5a, the variation of the uplift from the crest of the dome (with or without apical depression) is a function of the maximum uplift (*Y*-axis, corresponding to 100%) along a radial distance (*X*-axis; see inset in Fig. 5a). The profiles in Fig. 5b show close similarities with the ones with configuration A in Fig. 5a.

The experiments with configuration B thus show the same evolution and geometry as compared to the experiments with configuration A. This indicates that removing the basal cylinder of LSI does not change the overall evolution of the experiments at surface.

3.3. Evolution of the experiments with configuration C

The experiments with configuration C have a smaller ($\Delta\eta \approx 10^1$) viscosity contrast between the buoyant material and the embedding media (Fig. 1). The evolution of an experiment with configuration C is shown through a representative model (DOM 18; initial conditions in Fig. 1).

Fig. 6a shows a dome (6.4 cm wide and 3 mm high) with a flat apical part on the model surface after

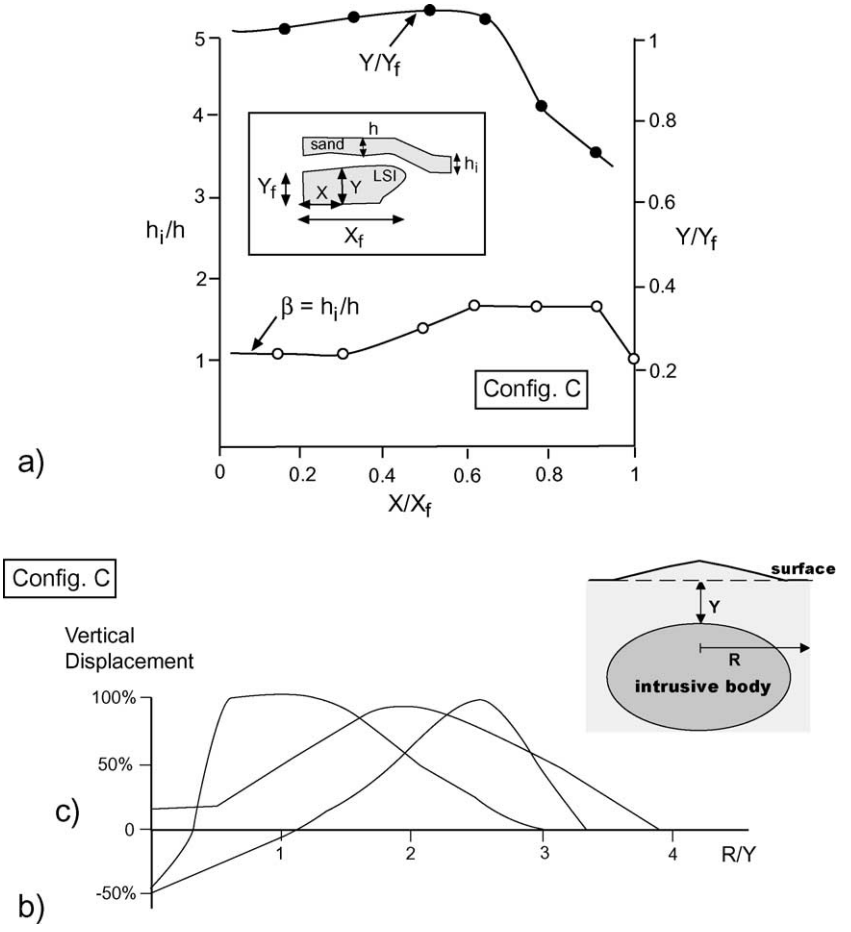

Fig. 7. (a) Relationships between intrusion emplacement and surface deformation in DOM 18. The deformation in the sand is expressed by the stretch parameter $\beta = h_i/h$. Shape variation of the intrusion is given by $\kappa = Y/Y_f$ (see note in Fig. 3 for more details). Measures taken from section in Fig. 5c. (b) Uplift profiles of half of the experimental domes with configuration C as a function of the distance from the centre of the dome. The uplift is normalized to the maximum uplift (100%) and the distance is normalized to the depth of the intrusion.

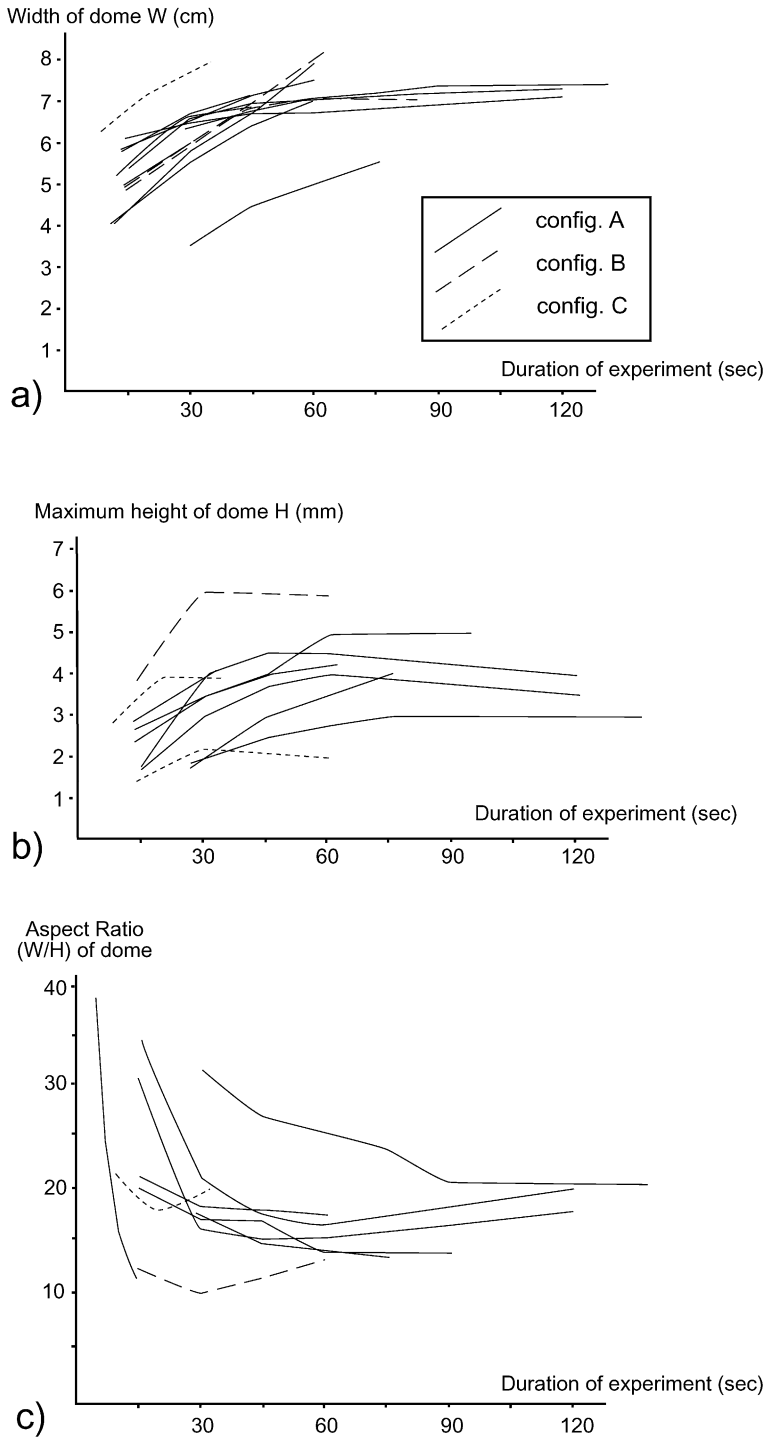

Fig. 8. (a) Variations of the width W of the domes with time in the experiments with configurations A, B and C. (b) Variations of the maximum height H of the dome with time. (c) Variations of the aspect ratio A of the domes with time.

15 s in the centrifuge. At 30 s, the dome (7.7 cm wide and 4 mm high) shows a broad depression (3.3 cm wide and 1.5 mm deep) (Fig. 6b). Any increase in the duration of the experiment does not change the deformation pattern at surface; the experiment thus reaches its stable configuration at $t = 30$ s. Fig. 6c shows a section view of the experiment at 30 s. The LSI has completely risen (at depth it has been replaced by the down flowing DSI) and spread at the base of the sand-pack, with a lens-shaped configuration; the floor of the intrusion shows a sag or downward convexity.

Fig. 7a shows the final variation in the thickness of the overburden and the intrusion in section view (data

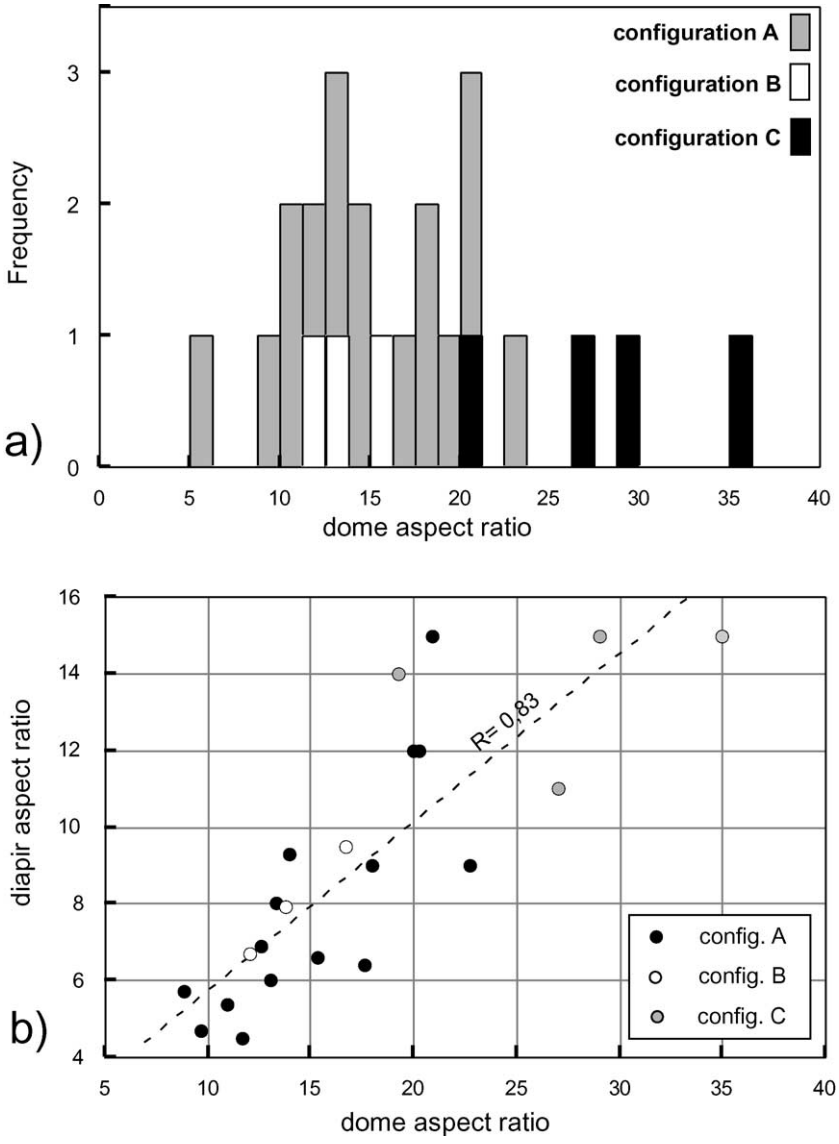

Fig. 9. (a) Aspect ratios of the domes at the final stage of deformation. (b) Diagram showing the positive correlation among the aspect ratios of the domes and of the underlying intrusions. The correlation indicates that $A_{dom} \approx 2A_{dia}$.

taken from Fig. 6c). The deformation in the sand is expressed by the stretch parameter $\beta = h_i/h$; shape variation of the intrusion is given by $\kappa = Y/Y_f$. The lens-shaped intrusion and the overburden are characterized by a broad central depression and a peripheral upward flexure. The central part of the intrusion is the thinnest, conversely to that observed in Fig. 3.

The remaining experiments with configuration C show a similar evolution. This consists of the development of a dome with a broad central depression (wider than half of the width of the dome), as a result of the emplacement of a lens-shaped intrusion. No extrusion of LSI has been observed, independently from the duration of the experiment. The normalized profiles of half of the experimental domes with configuration C

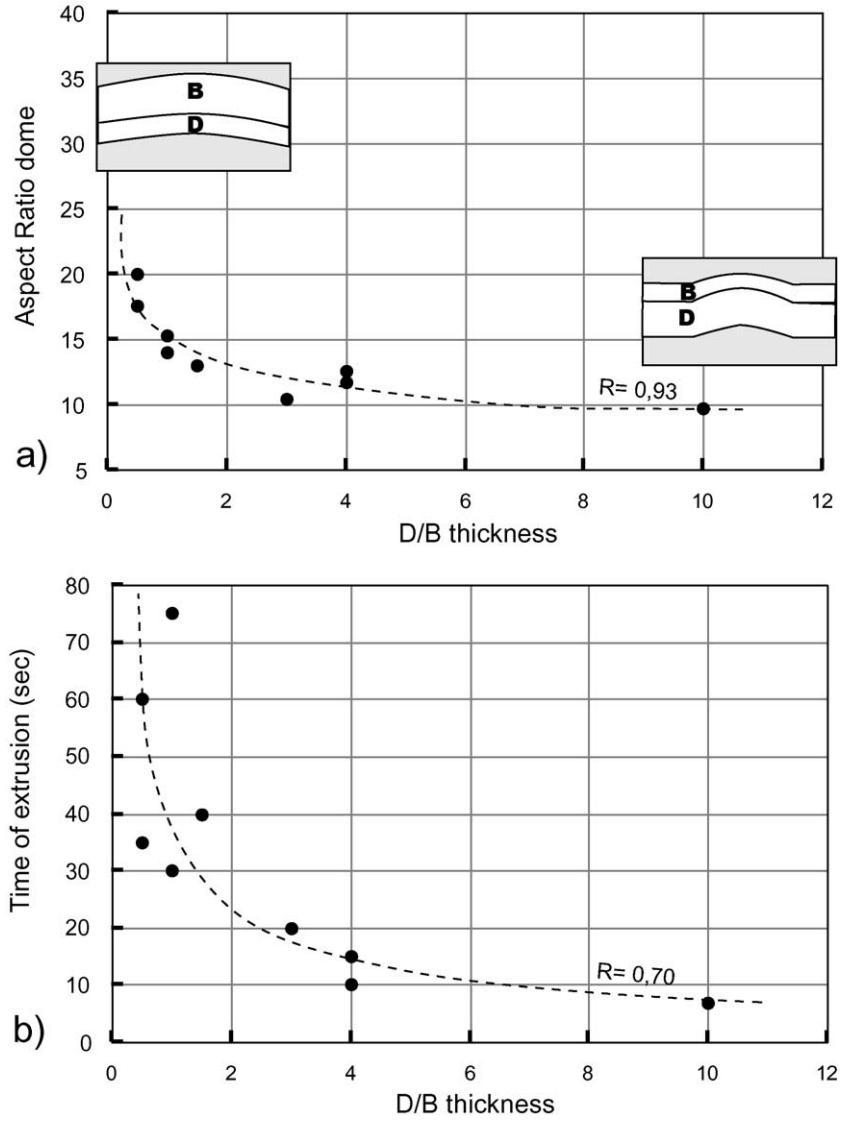

Fig. 10. (a) Inverse correlation between the aspect ratios of the domes and the ratio (D/B) between the thickness of the brittle and ductile layers (experiments with configuration A). (b) Inverse correlation between the time required to have silicone extrusion and the D/B ratio (experiments with configuration A).

at the final stage of deformation are shown in Fig. 7b. Again, the variation of the uplift from the crest of the dome is a function of the maximum uplift (y-axis, corresponding to 100%) along a radial distance (x-axis; see inset in Fig. 7b). The width and depth of the depression are larger, compared to the experiments with configurations A and B (Fig. 5); the maximum uplift is observed at the periphery of the dome.

3.4. General features of the experiments

The growth rate of the domes at surface is similar in all the configurations. The width W of the dome increases with time, reaching a limit at $W \sim 7$ cm, independent of the configuration (Fig. 8a). The maximum height H of the dome increases similarly, reaching a limit at $H \sim 4-6$ mm (Fig. 8b); several experiments show a decrease in the height of the dome at late stages, due to the development of the crestal depression. The aspect ratio A ($A = W/H$) of the domes decreases exponentially during doming (Fig. 8c), suggesting an increase in the height of the dome with regard to its width. Some domes show a slight increase in their aspect ratios at late stages, due to the decrease in height of the domes during the development of the depression (Fig. 8b).

Fig. 9a shows the distribution of the aspect ratios (W/H) of the domes at the final stage of deformation. The aspect ratios related to the domes in experiments with configurations A and B are between 9 and 20. The aspect ratios of the domes in the experiments with configuration C are between 19 and 35.

The aspect ratios of the domes (A_{dom}) are proportional to the aspect ratios of the underlying silicone diapirs (A_{dia} = width of intrusion/thickness of intrusion) in the final stage of deformation for the three adopted configurations (Fig. 9b). The data in Fig. 9b do not include the experiments without DSI (see experiment in Fig. 4), as here no major lateral spreading of the LSI occurs, since the sand confines the intrusion. The general correlation, characterized by $A_{dom} \approx 2A_{dia}$, indicates how the surface deformation is controlled by the shape (height and width) of the underlying intrusion. Fig. 9b also shows that the experiments with configuration C are characterized by intrusions with higher aspect ratios than the ones with configurations A and B, to which corresponds a higher aspect ratio of the dome (Fig. 9a). This shows that lens-shaped intrusions are responsible for wider and lower domes at surface.

The aspect ratio of the domes (configuration A) decreases with increasing the ratio between the thickness of the ductile and brittle layers D/B (Fig. 10a). Such correlation implies that domes with lower aspect ratio form with a thicker ductile layer; conversely, domes with higher aspect ratio form with a thicker brittle layer.

The time required to observe silicone extrusion in the experiments (configuration A) also decreases with the D/B ratio, as shown in Fig. 10b. The relation implies that a thick brittle layer limits extrusion; conversely, a thick ductile layer enhances extrusion.

4. Discussion

4.1. General evolution of the experiments

The experiments are characterized by the development of a dome, a depression (much broader in experiments with configuration C) on the top of the dome and, eventually and only in the experiments with configurations A and B, by silicone extrusion on the crest of the dome. A similar evolution was observed in experiments related to salt diapirism (Schultz Ela et al., 1993), laccolith emplacement (Roman Berdiel et al., 1995), laccolith emplacement in a centrifuge (Berner et al., 1972; Dixon and Simpson, 1987) and resurgent doming (Acocella et al., 2001).

The growth of the domes shows a pattern characterized by a high rate in the initial stages, followed by a decreasing rate in the final stages, as the underlying intrusion spreads laterally. Similar results were obtained in centrifuge by means of different materials and configurations (Dixon and Simpson, 1987). The comparison with our results thus indicates that, despite the different boundary conditions, the domal shape of the models at surface shows similar kinematics.

The growth of the dome is also controlled by the viscosity contrast between the intrusion and the overburden. The domes are higher in models with configuration A, as compared to configuration C, because the higher viscosity contrast between intrusion and

confining medium forces the intrusion to rise upwards rather than spread laterally.

The aspect ratio of the domes is also controlled by the ductile to brittle thickness ratio (Fig. 10a). This feature can be explained as due to changes in the flexural strength of the overburden above the rising buoyant material. In fact, a thicker sand pack (lower D/B) increases the flexural rigidity and thus the width of the dome and vice versa (Turcotte and Schubert, 1982, p. 120); as a consequence, different vertical displacement profiles are obtained in Figs. 5 and 7b. A similar control of the overburden thickness on the deformation was experimentally observed (Roman-Berdiel et al., 1995; Acocella et al., 2001).

A depression, narrower in models with configuration A and much broader in models with configuration C, forms on the dome. Its development was recognized in previous experiments (Withjack and Scheiner, 1982; Komuro, 1987; Mulugeta, 1985; Davison et al., 1993; Schultz-Ela et al., 1993; Marti et al., 1994; Acocella et al., 2001).

Stresses involved in the deformation of the overburden (thinning and development of the depression) are the bending and shear stresses acting below the sand during intrusion emplacement. The bending strain ε_f within a bent beam is proportional to the distance from the neutral plane y and inversely proportional to the radius of curvature R: $\varepsilon_f = y/R$ (Fig. 11). In the experiments, we calculated a bending strain of the order of $\varepsilon_f \sim 4\%$, caused by the doming alone (Acocella and Mulugeta, 2001). However, this, on its own, is not sufficient to account for the finite extension leading to the formation of the crestal depression. This suggests that thinning and stretching of the brittle layer by forceful intrusion emplacement are also necessary to account for the total finite extension, as suggested from dynamic models of narrow rifts (Mulugeta, 1985). The shear stresses acting below the sand must have exceeded its shear strength to account for the crestal depression. By comparison, for models of uniform elastic overburden above a laccolithic intrusion, the differential stress reaches a maximum value (and hence locus of failure) above the periphery of the intrusion (Pollard and Johnson, 1973).

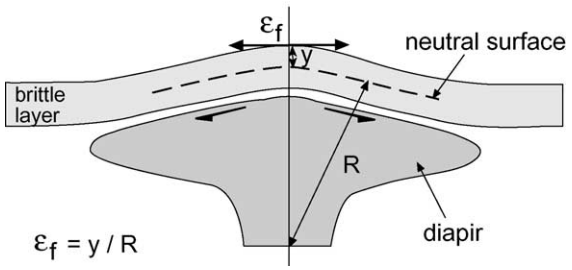

Fig. 11. Sketch showing deflection (radius R) of a brittle layer by a rising intrusion to generate bending strains ε_f at distance y from the neutral plane.

4.2. Intrusion shapes

The main differences observed in the experimental results are attributed to the adopted initial configurations. The experiments with configurations A and B show an evolution characterized by doming, the development of an apical depression and extrusion as a result of the spreading of a laccolith-like intrusion. However, the lateral spreading (and thus the laccolith shape) of the LSI occurs only if a lower viscosity layer (the DSI) is present. The experiments with configuration C are characterized by doming and sagging, forming a broad central depression, as a result of the spreading of a lens-shape intrusion beneath the brittle layer.

Figs. 3 and 7a show the differences between pluton emplacement and the surface deformation for the configurations A and C. In both models, the surface deformation (dome shape, depression geometry) is controlled by the emplacement dynamics of the subjacent plutons. In configuration A (Fig. 3), the intrusion is thicker in the central region. The β ratio in the sand is thus higher in the centre, inducing the apical depression. The emplacement of the intrusion (rise to the base of the brittle layer, lateral spreading and uplifting the overburden) and the domed shape of its roof and overburden show close similarities with the mechanism of emplacement and the shape of laccoliths (Fig. 12a; Corry, 1988).

Conversely, in configuration C (Fig. 7a) the pluton is thinner in the central part. This suggests a radial effect of material transport from the central region outwards. This thinning of the pluton in the centre seems to be responsible for the sagging of the overburden, inducing the broad depression. This also produced a slightly higher β ratio of the brittle overburden in the margins (Fig. 7a).

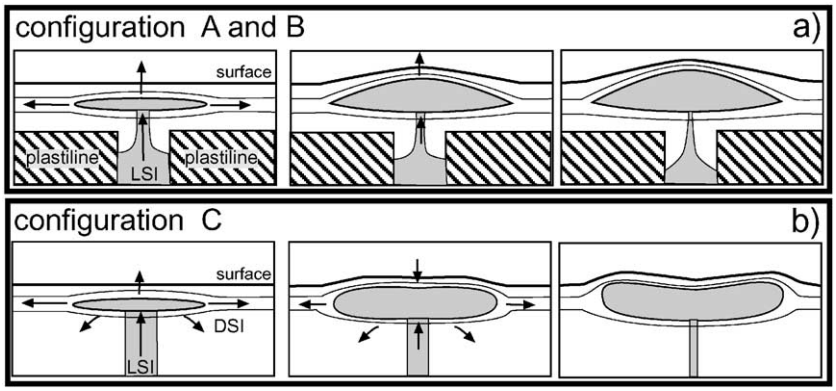

Fig. 12. (a) Schematic evolution of experiments with configuration A or B. Plastilina enhances the viscosity contrast between the intrusion (grey) and the embedding media, focusing the rise of the LSI in the central part. The space required to accommodate the emplacement therefore occurs through roof lifting. The intrusion has a laccolith shape. (b) Schematic evolution of experiments with configuration C. Plastilina is removed and, during the rise of the LSI, the DSI flows laterally downwards. The space required to accommodate the emplacement of the intrusion is here provided through roof lifting and downward flow of the embedding media. The resulting intrusion is a combination of a laccolith and a lopolith. The arrows schematically show the vectors of displacement of the materials, with a length proportional to the amount of transferred material.

The evolution of these experiments was enhanced by the lateral fall of the DSI and the denser overburden during rise of the buoyant layer. The downward flow of the surrounding material during the rise of the intrusion and the downsag of the floor of the intrusion imply that the emplacement partly occurred by means of floor depression, in a way similar to that proposed for lopoliths (Fig. 12b; Cruden, 1998, and references therein). The remaining space required to accommodate the intrusion was created by roof uplift or doming. Thus, the mechanism of emplacement of the intrusions with configuration C is a combination of floor depression (lopolith-like) and roof uplift (laccolith-like). The depression of the floor of the pluton limited roof uplift and therefore the rise and extrusion of silicone in the central part of the intrusion.

The different evolutions between configurations A or B and C depend upon the viscosity and/or the stiffness contrast between the intrusion and the surrounding media (Fig. 12). In the experiments with configuration A or B, plastilina, possessing a higher yield strength and viscosity, confines the rise of the buoyant layer and the fall of the DSI. Conversely, when the surrounding medium has near similar viscosity to the intrusion (configuration C), it enhances the lateral fall of the DSI during the rise of the buoyant layer; the DSI thus replaces the space vacated by the rising intrusion.

4.3. Comparison with nature

Considering the imposed experimental conditions, the models find their best natural examples in viscous plutons emplaced at shallow crustal levels and in subvolcanic intrusions (i.e., felsic magma chambers). The experiments showed that roof uplift and, subsequently, floor depression can accommodate the required space during pluton emplacement at shallow crustal levels. The conditions leading to the formation of a laccolith (roof uplift) or a lopolith (floor depression) are usually related to the depth of the emplacement. Between the two, roof uplift should occur at shallower crustal levels, whereas floor depression should occur at deeper crustal levels (Cruden, 1998, and references therein). The dependence of the mechanism of emplacement (laccolith or laccolith–lopolith hybrid) upon the viscosity/strength contrast between the intrusion and the embedding media shown by the experiments may be a further parameter controlling space accommodation during pluton emplacement.

Roof uplift due to laccolith-like intrusions is a common mechanism of pluton emplacement at shallow crustal levels (Scaillet et al., 1995; Brown and Solar, 1998; Morgan et al., 1998; Quirk et al., 1998; Acocella, 2000). This might be due to the very limited mass transfer recognized around the roots of a rising intrusion (Marsh, 1982; Mahon et al., 1988; Schmeling et

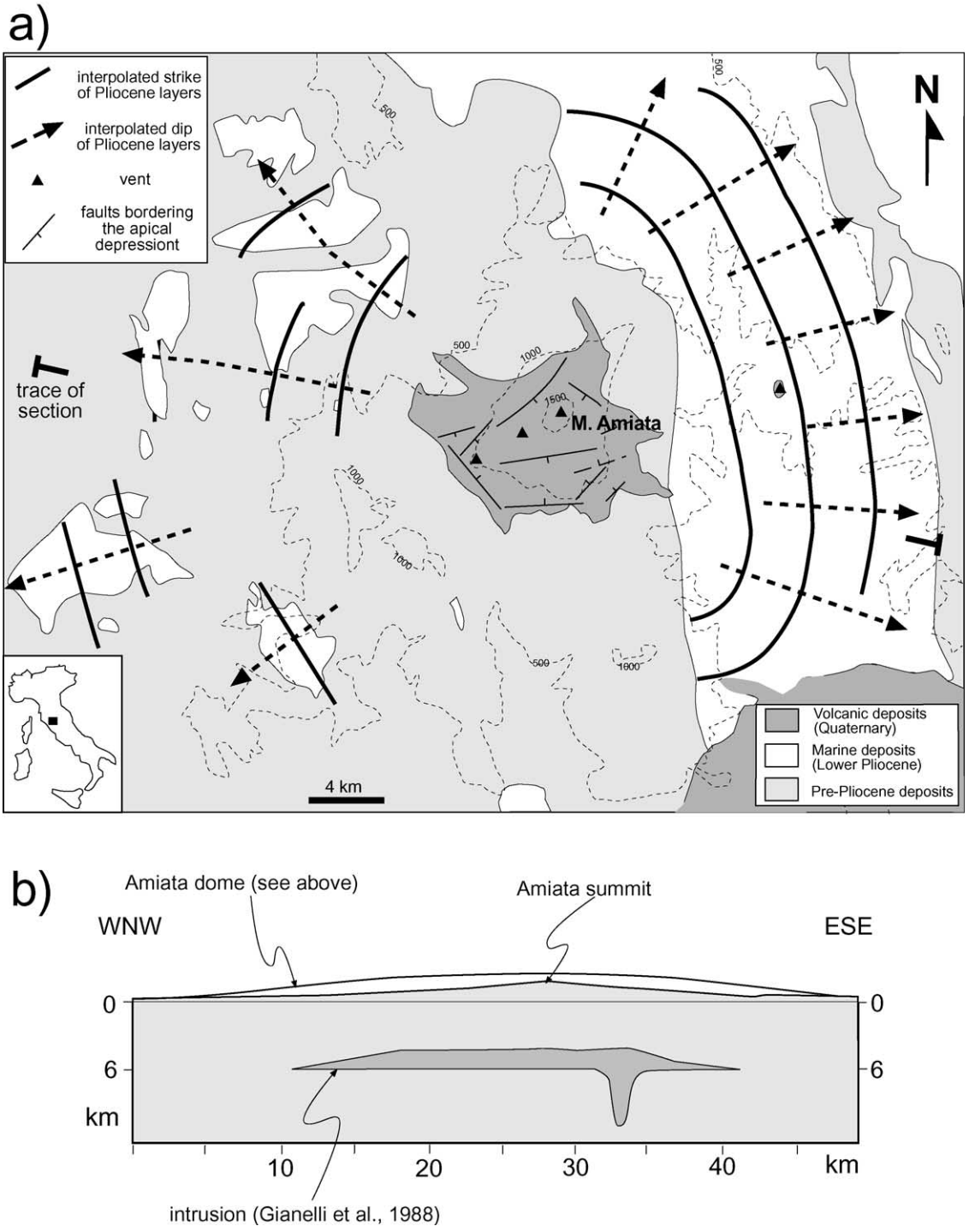

Fig. 13. (a) Interpolation of the attitudes of the Pliocene deposits in the Amiata area. Solid lines refer to the mean strike of the layers; dashed lines refer to their mean dip direction. The lines highlight a dome centred on the volcanics of M. Amiata. (b) Schematic section along Amiata, showing the roof of the intrusion, as inferred from gravity data and the domed overburden (modified after Acocella, 2000).

al., 1988; Paterson and Fowler, 1993; Paterson and Miller, 1998; Tikoff et al., 1999): as a result, the higher viscosity contrast between the intrusion and the embedding medium may favour the formation of laccoliths.

The common occurrence of significant erosion above most intrusions limits a broad comparison of the experimental results with nature. Among the best examples of preserved surface deformations induced by pluton emplacement is the Amiata area (Italy). During the Pliocene, the Amiata area was uplifted due to pluton emplacement (Gianelli et al., 1997, and references therein). Pleistocene volcanics filled a previously formed depression within the uplifted area (Calamai et al., 1970; Ferrari et al., 1996). The shape and granitoid composition of the buried intrusion are constrained by gravity and the volcanics petrology (Gianelli et al., 1988; Orlando et al., 1994; Gianelli et al., 1997).

The interpolation of the attitudes of the Lower Pliocene marine sediments (deposited immediately before the uplift) within the uplifted area highlights a dome centered on the volcanics of M. Amiata (Fig. 13a). The WNW–ESE section in Fig. 13b combines the field with the gravity data, suggesting that the dome is the result of the overburden deformation due to pluton emplacement (Acocella, 2000). The evidence for roof uplift due to a tabular intrusion suggests a laccolith-like pluton, similarly to that observed in the experiments with configuration A. The apical depression is the result of the crustal stretching due to doming and to the forceful emplacement of the intrusion, which were large enough to induce failure in the upper crust (Acocella and Mulugeta, 2001).

The comparison between the experiments and the Amiata case (1) confirms that roof uplift is an important means of making space during shallow pluton emplacement and (2) suggests that, where roof uplift plays a major role, pluton emplacement at shallow levels can induce a well-correlated sequence of events at surface: doming, the development of an apical depression and crestal extrusion.

As far as lopoliths are concerned, a limited amount has been recognized on the field (Cruden, 1998, and references therein). Even tough at a larger scale (10^2–10^3 km), a natural example of the configuration C models can be the Victoria Lake region in the East African Rift System. The central depression (Lake Victoria), bordered by uplifted areas (the branches of the East African Rift System), is in fact due to the ascent of a mantle plume with a moderate viscosity contrast with the embedding media (Griffith and Campbell, 1991).

5. Conclusions

The model results show the effect of density and viscosity contrast in the dynamics of pluton emplacement and their impact in deformation of the overburden. When there is a marked viscosity contrast ($\Delta\eta \approx 10^{2-4}$) between intrusion and surrounding media, doming and thinning of the overburden leads to the development of an apical depression followed by extrusion within the depression. The intrusion has a laccolith-like shape.

In contrast, when there is little viscosity contrast ($\Delta\eta \approx 10^{1}$) between intrusion and overburden, a broad depression develops in the central region and an upward flexure towards the periphery. The intrusion is a hybrid between a laccolith and a lopolith. The comparison with the Amiata (Italy) case confirms roof uplift as an important means of accommodating space during pluton emplacement and suggests that pluton emplacement can induce a well-correlated sequence of events at surface.

Acknowledgements

The analogue experiments were conducted at the Hans Ramberg Tectonic Laboratories (Uppsala, Sweden), while VA benefited from a PhD grant at the University of Siena (Italy). The authors wish to thank A. Lazzarotto and C. Talbot for their encouragement and helpful discussions, H. Koyi for fruitful discussions, T. Tentler for helping in the experimental set-up and the reviewers A.R. Cruden and O. Merle for their useful comments. This work was financed by C.N.R. funds (responsible A. Lazzarotto, University of Siena).

References

Acocella, V., 2000. Space accommodation by roof lifting during pluton emplacement at Amiata (Italy). Terra Nova 12, 149–155.

Acocella, V., Mulugeta, G., 2001. Surface deformation induced by pluton emplacement: the case of Amiata (Italy). Phys. Chem. Earth 26, 355–362.

Acocella, V., Cifelli, F., Funiciello, R., 2001. The architecture of resurgent domes: insights from analogue models. J. Volcanol. Geotherm. Res. 111, 137–153.

Bateman, R., 1984. On the role of diapirism in the segregation, ascent and final emplacement of granitoid magmas. Tectonophysics 110, 211–231.

Benn, K., Odonne, F., de Saint Blanquat, M., 1998. Pluton emplacement during transpression in brittle crust: new views from analogue experiments. Geology 26, 1079–1082.

Berner, H., Ramberg, H., Stephansson, O., 1972. Diapirism in theory and experiment. Tectonophysics 15, 197–218.

Bittner, D., Schmeling, H., 1995. Numerical modelling of melting processes and induced diapirism in the lower crust. Geophys. J. Int. 123, 59–70.

Brown, M., 1994. The generation, segregation, ascent and emplacement of granite magma: the migmatite to crustally-derived granite connection in thickened orogens. Earth Sci. Rev. 36, 83–130.

Brown, M., Solar, G.G., 1998. Granite ascent and emplacement during contractional deformation in convergent orogens. J. Struct. Geol. 20, 1365–1393.

Brun, J.P., Pons, J., 1981. Strain patterns of pluton emplacement in a crust undergoing non-coaxial deformation, Sierra Morena, Southern Spain. J. Struct. Geol. 3, 219–229.

Calamai, A., Cataldi, R., Squarci, P., Taffi, L., 1970. Geology, geophysics and hydrogeology of the Monte Amiata geothermal fields. Geotherm. Spec. Issue, 1–9.

Castro, A., 1987. On granitoid emplacement and related structures. A review. Geol. Rundsch. 76, 101–124.

Corry, C.E., 1988. Laccoliths; mechanics of emplacement and growth. Spec. Pap. Geol. Soc. Am. 220, 1–110.

Cruden, A.R., 1990. Flow and fabric development during the diapiric rise of magma. J. Geol. 98, 681–698.

Cruden, A.R., 1998. On the emplacement of tabular granites. J. Geol. Soc., London 155, 853–862.

Davison, I., Insley, M., Harper, M., Weston, P., Blundell, D., McClay, K., Quallington, A., 1993. Physical modelling of overburden deformation around salt diapirs. Tectonophysics 228, 255–274.

Dixon, J.M., 1975. Finite strain and progressive deformation in models of diapiric structures. Tectonophysics 28, 89–124.

Dixon, J.M., Simpson, D.G., 1987. Centrifuge modelling of laccolith intrusion. J. Struct. Geol. 9, 87–103.

D'Lemos, R.S., Brown, M., Strachan, R.A., 1992. Granite magma generation, ascent and emplacement within a transpressional orogen. J. Geol. Soc., London 149, 487–490.

Donnadieu, F., Merle, O., 1998. Experiments on the indentation process during cryptodome intrusions: new insights into Mount St. Helens deformation. Geology 26, 79–82.

Ferrari, L., Conticelli, S., Burlamacchi, L., Manetti, P., 1996. Volcanological evolution of the Monte Amiata, Southern Tuscany: new geological and petrochemical data. Acta Vulcanol. 8, 41–56.

Gianelli, G., Puxeddu, M., Batini, F., Bertini, G., Dini, I., Pandeli, E., Nicolich, R., 1988. Geological model of a young volcano-plutonic system: the geothermal region of Monte Amiata (Tuscany, Italy). Geothermics 17, 719–734.

Gianelli, G., Manzella, A., Puxeddu, M., 1997. Crustal models of the geothermal areas of southern Tuscany (Italy). Tectonophysics 281, 221–239.

Glazner, A., 1991. Plutonism, oblique subduction and continental growth: an example from the Mesozoic of California. Geology 19, 784–786.

Griffith, R.W., Campbell, I.H., 1991. Interaction of mantle plume heads with the Earth's surface and onset of small scale convection. J. Geophys. Res. 96, 18295–18310.

Grocott, J., Garde, A.A., Chadwick, B., Cruden, A.R., Swager, C., 1999. Emplacement of rapakivi granite and syenite by floor depression and roof uplift in the Palaeoproterozoic Ketilidian orogen, South Greenland. J. Geol. Soc., London 156, 15–24.

Guglielmo, G., 1993. Interference between pluton expansion and non-coaxial tectonic deformation: three dimensional computer model and field implications. J. Struct. Geol. 15, 593–608.

Hailemariam, H., Mulugeta, G., 1998. Temperature-dependent rheology of bouncing putties used as rock analogs. Tectonophysics 294, 131–141.

Hanson, R.B., Glazner, A.F., 1995. Thermal requirements for extensional emplacement of granitoids. Geology 23, 213–216.

Hogan, J.P., Price, J.D., Gilbert, M.C., 1998. Magma traps and driving pressure: consequences for pluton shape and emplacement in an extensional regime. J. Struct. Geol. 20, 1155–1168.

Hubbert, M.K., 1937. Theory of scale models as applied to the study of geologic structures. Bull. Geol. Soc. Am. 48, 1459–1520.

Hutton, D.H.W., 1988. Granite emplacement mechanisms and tectonic controls: inferences from deformation studies. Trans. R. Soc. Edinb. Earth Sci. 79, 245–255.

Komuro, H., 1987. Experiments on cauldron formation: a polygonal cauldron and ring fractures. J. Volcanol. Geotherm. Res. 31, 139–149.

Krantz, R.W., 1991. Measurements of friction coefficients and cohesion for faulting and fault reactivation in laboratory models using sand and sand mixtures. In: Cobbold, P.R. (Ed.), Experimental and Numerical Modelling of Continental Deformation. Tectonophysics 188, 203–207.

Lipman, P.W., 1984. The roots of ash flow calderas in Western North America: windows into the tops of granitic batholiths. J. Geophys. Res. 89, 8801–8841.

Mahon, K.I., Harrison, T.M., Drew, D.A., 1988. Ascent of a granitoid diapir in a temperature varying medium. J. Geophys. Res. 93, 1174–1188.

Mandl, G., De Jong, L.N.J., Maltha, A., 1977. Shear zones in granular material. Rock Mech. 9, 95–144.

Marsh, B.D., 1982. On the mechanics of igneous diapirism, stoping and zone melting. Am. J. Sci. 282, 808–855.

Marti, J., Ablay, G.J., Redshaw, L.T., Sparks, R.S.J., 1994. Experimental studies of collapse calderas. J. Geol. Soc. London 151, 919–929.

McCaffrey, K.J.W., 1992. Igneous emplacement in a transpressive shear zone: Ox Mountains igneous complex. J. Geol. Soc., London 149, 221–235.

Merle, O., 1998. Internal strain within lava flows from analogue modelling. J. Volcanol. Geotherm. Res. 81, 189–206.

Merle, O., Vendeville, B., 1995. Experimental modelling of thin-skinned shortening around magmatic intrusions. Bull. Volcanol. 57, 33–43.

Morgan, S.S., Law, R.D., Nyman, M.W., 1998. Laccolith-like emplacement model for the Papoose Flat pluton based on porphyroblast matrix analysis. Geol. Soc. Am. Bull. 110, 96–110.

Mulugeta, G., 1985. Dynamic models of continental rift valley systems. Tectonophysics 113, 49–73.

Orlando, L., Bernabini, M., Bertini, G., Cameli, G.M., Dini, I., 1994. Interpretazione preliminare del minimo gravimetrico del Monte Amiata. Studi Geol. Camerti 1, 175–181.

Paterson, S.R., Vernon, R.H., Tobisch, O.T., 1989. A review of criteria for identification of magmatic and tectonic foliations in granitoids. J. Struct. Geol. 11, 349–363.

Paterson, S.R., Fowler, T.K., 1993. Re-examining pluton emplacement processes. J. Struct. Geol. 15, 191–206.

Paterson, S.R., Miller, R.B., 1998. Magma emplacement during arc-perpendicular shortening: an example from the Cascades crystalline core, Washington. Tectonics 17, 571–586.

Petford, N., Atherton, M.P., 1992. Granitoid emplacement and deformation along a major crustal lineament: the Cordillera Blanca, Peru. Tectonophysics 205, 171–185.

Pitcher, W.S., 1979. The nature, ascent and emplacement of granitic magmas. J. Geol. Soc., London 136, 627–662.

Pollard, D.D., Johnson, A.M., 1973. Mechanics of growth of some laccolithic intrusions in the Henry Mountains, Utah, II. Tectonophysics 18, 311–354.

Quirk, D.G., D'Lemos, R.S., Mulligan, S., Rabti, M.R., 1998. Insights into the collection and emplacement of granitic magma based on 3D seismic images of normal fault-related salt structures. Terra Nova 10, 268–273.

Ramberg, H., 1981. Gravity, Deformation and the Earth's Crust in Theory, Experiments and Geological Applications. Academic Press, London.

Ramsay, J.G., 1989. Emplacement kinematics of a granite diapir: the Chindamora batholith, Zimbabwe. J. Struct. Geol. 11, 191–209.

Roman-Berdiel, T., Gapais, D., Brun, J.P., 1995. Analogue models of laccolith formation. J. Struct. Geol. 17, 1337–1346.

Roman-Berdiel, T., Gapais, D., Brun, J.P., 1997. Granite intrusion along strike-slip zones in experiments and nature. Am. J. Sci. 297, 651–678.

Rubin, A.M., 1993. Dikes vs. diapirs in viscoelastic rock. Earth Planet. Sci. Lett. 119, 641–659.

Scaillet, B., Pecher, A., Rochette, P., Champenois, M., 1995. The Gangotri granite (Garhwal Himalaya): laccolithic emplacement in an extending collisional belt. J. Geophys. Res. 100, 585–607.

Schellart, W.P., 2000. Shear test results for cohesion and friction coefficients for different granular materials: scaling implications for their usage in analogue modelling. Tectonophysics 324, 1–16.

Schmeling, H., Cruden, A.R., Marquart, G., 1988. Finite deformation in and around a fluid sphere moving through a viscous medium: implications for diapiric ascent. Tectonophysics 149, 17–34.

Schultz-Ela, D.D., Jackson, M.P.A., Vendeville, B.C., 1993. Mechanics of active salt diapirism. Tectonophysics 228, 275–312.

Shaw, H.R., 1985. Links between magma-tectonic rate balances, plutonism and volcanism. J. Geophys. Res. 90, 11275–11288.

Talbot, C.J., 1999. Can field data constrain rock viscosities? J. Struct. Geol. 21, 949–957.

Tikoff, B., Teyssier, C., 1992. Crustal-scale, en echelon "P shear" tensional bridges: a possible solution to the batholithic room problem. Geology 20, 927–930.

Tikoff, B., de Saint Blanquat, M., 1997. Transpressional shearing and strike-slip partitioning in the Late Cretaceous Sierra Nevada magmatic arc, California. Tectonics 16, 442–459.

Tikoff, B., de Saint Blanquat, M., Teyssier, C., 1999. Translation and the resolution of the pluton space problem. J. Struct. Geol. 21, 1109–1117.

Tobisch, O., Cruden, A.R., 1995. Fracture controlled magma conduits in an obliquely convergent continental magmatic arc. Geology 23, 941–944.

Turcotte, D.L., Schubert, G., 1982. Geodynamics: Application of Continuum Physics to Geological Problems. Wiley, NY, 450 pp.

Vigneresse, J.L., 1995. Crustal regime of deformation and ascent of granitic magma. Tectonophysics 249, 187–202.

Weinberg, R.F., Podladchikov, Y., 1995. The rise of solid-state diapirs. J. Struct. Geol. 17, 1183–1195.

Whitehead, J.A., Luther, D.S., 1975. Dynamics of laboratory diapir and plume models. J. Geophys. Res. 80, 705–717.

Wilson, J., Grocott, J., 1999. The emplacement of the granitic Las Tazas complex, northern Chile: the relationship between local and regional strain. J. Struct. Geol. 21, 1513–1523.

Withjack, M.O., Scheiner, C., 1982. Fault patterns associated with domes; an experimental and analytical study. AAPG Bull. 66, 302–316.

Yoshida, T., 2001. The evolution of arc magmatism in the NE Honshu Arc, Japan. Tohoku Geophys. J. 36, 131–149.